Report on Landsat 8 and Sentinel-2B observations of the Nord Stream 2 pipeline methane leak

Matthieu Dogniaux[1], Joannes D. Maasakkers[1], Daniel J. Varon[2] and Ilse Aben[1]

[1]SRON Netherlands Institute for Space Research, Leiden, The Netherlands

[2]School of Engineering and Applied Science, Harvard University, Cambridge, USA

Corresponding author: Matthieu Dogniaux

Email: M.Dogniaux@sron.nl

Report on Landsat 8 and Sentinel-2B observations of the Nord Stream 2 pipeline methane leak

Matthieu Dogniaux[a], Joannes D. Maasakkers[a], Daniel J. Varon[b], Ilse Aben[a]

[a] *SRON Netherlands Institute for Space Research, Leiden, The Netherlands*
[b] *School of Engineering and Applied Science, Harvard University, Cambridge, 02138, USA*

Abstract

In late September 2022, explosions of the Nord Stream pipelines caused what could be the largest anthropogenic methane leak ever recorded. We report on Landsat 8 (L8) and Sentinel-2B (S-2B) observations of the sea foam patch produced by the Nord Stream 2 (NS2) leak located close to Bornholm Island, acquired on September 29th and 30th, respectively. Usually, reflected sunlight over sea is insufficient for these Earth-imagers to observe any methane signal in nadir-vewing geometry. However, the NS2 foam patch observed here is bright enough to possibly allow the detection of methane above it. We apply the Multi-Band Single-Pass (MBSP) method to infer methane enhancement above the NS2 foam patch and then use the Integrated Mass Enhancement (IME) method in an ensemble approach to estimate methane leak rates and their uncertainties. This very specific NS2 observation case challenges some of MBSP and IME implicit hypotheses, and thus calls for customized calibrations: (1) for MBSP, we perform an empirical calibration of sea foam albedo spectral dependence by using sea foam observations in ship trails, and (2) for IME, we yield a tailored effective wind speed calibration that accounts for a partial plume observation, as methane enhancement may only be seen above the NS2 sea foam patch. Due to large uncertainties, no firm conclusion can be drawn from the single overpasses of L8 and S-2B. However, if we opportunistically assume that the L8 and S-2B methane leak rates are independent, we obtain a positive leak detection with a weak confidence, showing an averaged dual-overpass (L8 and S-2B combined) NS2 methane leak rate of 415 ± 321 t/hr. Overall, our work illustrates how implicit method hypotheses need to be considered and compensated for in unusual observation cases such as this one.

---

1. Introduction

From September 26^{th} to October 2^{nd}, 2022, leaks occurred on the Nord Stream (NS) and Nord Stream 2 (NS2) pipelines in the Baltic Sea. They caused intensive bubbling and extensive foam patches at the sea surface, as well as methane emissions that could be one of the strongest methane leak events ever recorded (Sanderson, 2022). The Southern NS2 sea foam patch close to Bornholm Island was observed on September 29^{th} and 30^{th} by Landsat 8 and Sentinel-2B (respectively), two Earth-imaging satellites that are sensitive to large methane point sources (Varon et al., 2021). We report on those two observations, and exhibit the challenges they come with to evaluate the NS2 methane leak rate.

Anthropogenic methane emissions are the second largest contributor to human-induced climate change, and their drastic reduction is required to keep global warming below 1.5°C or 2.0°C (IPCC, 2021). In the past decade, developments in space-based methane observation have had a transformative impact on methane super-emitter detection and monitoring, and can contribute to track progress towards the Paris Agreement goals (e.g. Nisbet et al., 2020). Among them, the TROPOspheric Monitoring Instrument (TROPOMI, Veefkind et al., 2012; Lorente et al., 2021) measures back-scattered sunlight in the short-wave infrared (SWIR) around 2.3 μm at 0.25 nm resolution, at a moderate 5.5×7 km^2 spatial resolution at nadir and with daily global coverage. Global methane concentrations maps are drawn from these measurements using a full-physics approach which accounts for geophysical variables besides methane (e.g. albedo, water vapour, aerosol optical depth, etc) that could interfere in the retrieval process (Lorente et al., 2021). Its observations have been successfully used to detect and estimate anthropogenic methane emissions arising from various point or localized sources (e.g. Pandey et al., 2019; Lauvaux et al., 2022; Schuit et al., 2023). SWIR satellite instruments with higher spatial resolution (few tens of meters) have proved complementary by enabling the identification of methane emission sources at facility-scale. These notably include the methane-dedicated GHGSat constellation (Jervis et al., 2021) and Earth-imagers such as Sentinel-2 or Landsat 8. Earth-imagers are not spectrally resolved like TROPOMI and were not originally designed to measure greenhouse gases. However, under the right conditions (bright, quasi-homogeneous land surface), their methane sensitive bands ($\sim$ 100-200 nm in width) can be repurposed to retrieve large methane concentration enhancements and image point source emission plumes (e.g. Varon et al., 2021; Irakulis-Loitxate et al., 2022b). Like any other SWIR instrument, these Earth-imagers do not typically offer coverage over water bodies, because the water albedo is too dark at nadir pointing. However, sun-glint observations over sea can allow methane plume detection with these satellites as well (Irakulis-Loitxate et al., 2022a).

When the NS and NS2 leaks occurred, and in the following week, TROPOMI was not able to acquire exploitable data over land in the Baltic Sea vicinity due to cloudiness. However, thanks to their finer spatial resolution, Landsat 8 (L8) and Sentinel-2B (S-2B) have been able to perform nadir-pointing observations showing the Southern NS2 leak on September 29th and 30th, respectively. They did not benefit from sun glint, but the bright foam patch produced by the bubbling leak at the sea surface reflected enough sunlight to consider using the observations, and assess whether a methane signal can be sensed. Besides L8 and S-2B, GHGSat could point their instruments towards the same NS2 leak on September 30th and observe a methane emission plume in glint geometry twice (GHGSat, 2022). After initial Twitter reports by the International Methane Emissions Observatory (IMEO, 2022), Jia et al. (2022) published results for the Sentinel-2B observation, acknowledging significant uncertainties in their methodology regarding the spectral reflectance of bubbles and the partial imaging of the methane plume.

This work first aims to show how Landsat 8 and Sentinel-2B observations of the Nord Stream 2 leak challenge implicit hypotheses in methods usually applied for Earth-imager methane plume analysis and emission rate quantification. It then proposes to account for identified issues by using customized calibrations, and to assess the possibility of using Landsat 8 and Sentinel-2B to sense and quantify methane emissions from the Nord Stream 2 leak.

2. Materials and methods

This section describes general aspects of the Landsat 8 and Sentinel-2B satellite data used here, and the generic (commonly applied) methane retrieval and emission rate quantification methods applied to process them.

2.1. Landsat 8 and Sentinel-2B satellite observations

Landsat 8 (hereafter L8) is an Earth-imaging satellite with a swath of 185 km and a revisit time of 16 days. It measures reflected sunlight over 10 different spectral bands located in the visible, short-wave infrared (SWIR) and thermal infrared, with spatial resolutions ranging from 15 to 100 m (Roy et al., 2014).

The Copernicus Sentinel-2 mission comprises two Earth-imaging satellites (Sentinel-2A and Sentinel-2B, hereafter S-2B) with a swath of 290 km and revisit time of 10 days each, and aims to monitor changes on our Earth's surface. They measure reflected sunlight over 12 different spectral bands located in the visible and SWIR, with spatial resolutions ranging from 10 to 60 m (Drusch et al., 2012).

Here, we use Top Of the Atmosphere (TOA) reflectance data observed by L8 and S-2B for two methane sensitive SWIR spectral bands around 1.6 μm (bands 6 and 11 for L8 and S-2B, respectively) and 2.2 μm (bands 7 and 12 for L8 and S-2B, respectively). These L8 and S-2B SWIR observations have spatial resolutions of 30 and 20 m, respectively.

2.2. Methane enhancement retrieval: the Multi-Band Single-Pass (MBSP) method

The TOA reflectance data can be used to retrieve atmospheric methane concentration enhancements with the Multi-Band Single-Pass (MBSP) method, first proposed by Varon et al. (2021). It relies on the relative change in TOA reflectance ΔR between two spectral bands s_1 (around 1.6 μm, low sensitivity to methane) and s_2 (around 2.2 μm, strong sensitivity to methane) computed as:

$$\Delta R = \frac{c \times s_2 - s_1}{s_1} \tag{1}$$

with c, a linear calibration coefficient fitted on all the pixels included in the target image, to account for any non-methane-related spectral effects between bands s_1 and s_2, most importantly the spectral dependence of the albedo. This calibration strategy implicitly assumes that image-wide pixels are representative of the surface characteristics expected below the (potential) methane plume. The rationale of MBSP is that deviations in the methane-sensitive s_2 band from the expected s_1/s_2 ratio (captured in the fitted c coefficient) are interpreted as methane enhancements. Pixels with $\Delta R < 0$ relate to higher than expected atmospheric absorption and yield positive methane enhancements. The translation of ΔR to methane enhancements is performed using pre-computed look-up tables, generated through radiative transfer simulations.

2.3. Emission rate quantification: the Integrated Mass Enhancement (IME) method

If a plume is observed in the image resulting from MBSP, the associated emission rate can be quantified using the Integrated Mass Enhancement

(IME) method. This method was first proposed by Frankenberg et al. (2016) and its calibration and operational use was improved by Varon et al. (2018). Given a plume, the IME method relates the emission rate Q to the plume's total methane mass and its residence time in the atmosphere. We have:

$$Q = \frac{U_{\text{eff}}}{L} \sum_i \Delta \mathrm{X}_{\mathrm{CH}_4 i} \times a_i \tag{2}$$

with U_{eff}, the effective wind speed transporting the plume, $L = \sqrt{\sum_i a_i}$ the plume length, $\mathrm{X}_{\mathrm{CH}_4 i}$, the total column methane enhancement of the i-th plume mask pixel, and a_i, the area of this pixel.

Plume transport includes complicated three-dimensional and turbulent effects that require computer-intensive simulations to be accounted for, if even possible given the randomness of turbulence. Through IME, the overall impacts of those effects are presumably captured into a single effective wind speed, denoted U_{eff}. U_{eff} is calibrated against the 10-m wind speed provided by meteorological models ($U_{10\text{m}}$) over a set of Large Eddy Simulations (LES) made for known synthetic emission rates, and re-sampled according to a given instrument characteristics (spatial resolution, noise model, etc.). Varon et al. (2021) provide an effective wind speed calibration model for Sentinel-2-like Earth imagers: $U_{\text{eff}} = 0.33 \times U_{10\text{m}} + 0.45$. Using this effective wind speed calibration implicitly assumes that the plume is observed in the same conditions as those used for the LES calibration, including for instance that the full extent of the plume is visible as per the given instrument sensitivity.

3. Two-fold custom calibration for the specific case of Landsat 8 and Sentinel-2B observations of the Nord Stream 2 leak

L8 and S-2B observations of the NS2 methane leak challenge some of the MBSP and IME implicit hypotheses, thus requiring tailored calibrations. This section first describes L8 and S-2B observations of the NS2 leak, and then details the specific calibrations.

3.1. Landsat 8 and Sentinel-2B observations of the Nord Stream 2 leak

Figure 1 shows L8 and S-2B TOA reflectance observations of the NS2 methane leak (top panels) and exhibits, using simple thresholds (see Supplements), the different pixel types (dark still sea, NS2 leak, cloud) included in the images by comparing s_1 and s_2 TOA reflectance values (bottom panels). The L8 image acquired on September 29th, 2022, is composed of the bubbling sea foam patch at its center, surrounded by dark still sea and cloud pixels. The S-2B image acquired on September 30th, 2022 is much cleaner and only includes the NS2 bubbling sea foam patch at its center, surrounded by dark still sea pixels.

3.2. Empirical calibration of the spectral dependence of sea foam reflectance in MBSP

Here, we seek to determine whether a methane enhancement signal can be retrieved from L8 and S-2B images of the NS2 sea foam patch. No methane signal can be expected to be visible over the dark still sea or the clouds. Consequently, considering the general description of MBSP given in Sect. 2.2, properly constraining the spectral dependence of sea foam albedo between

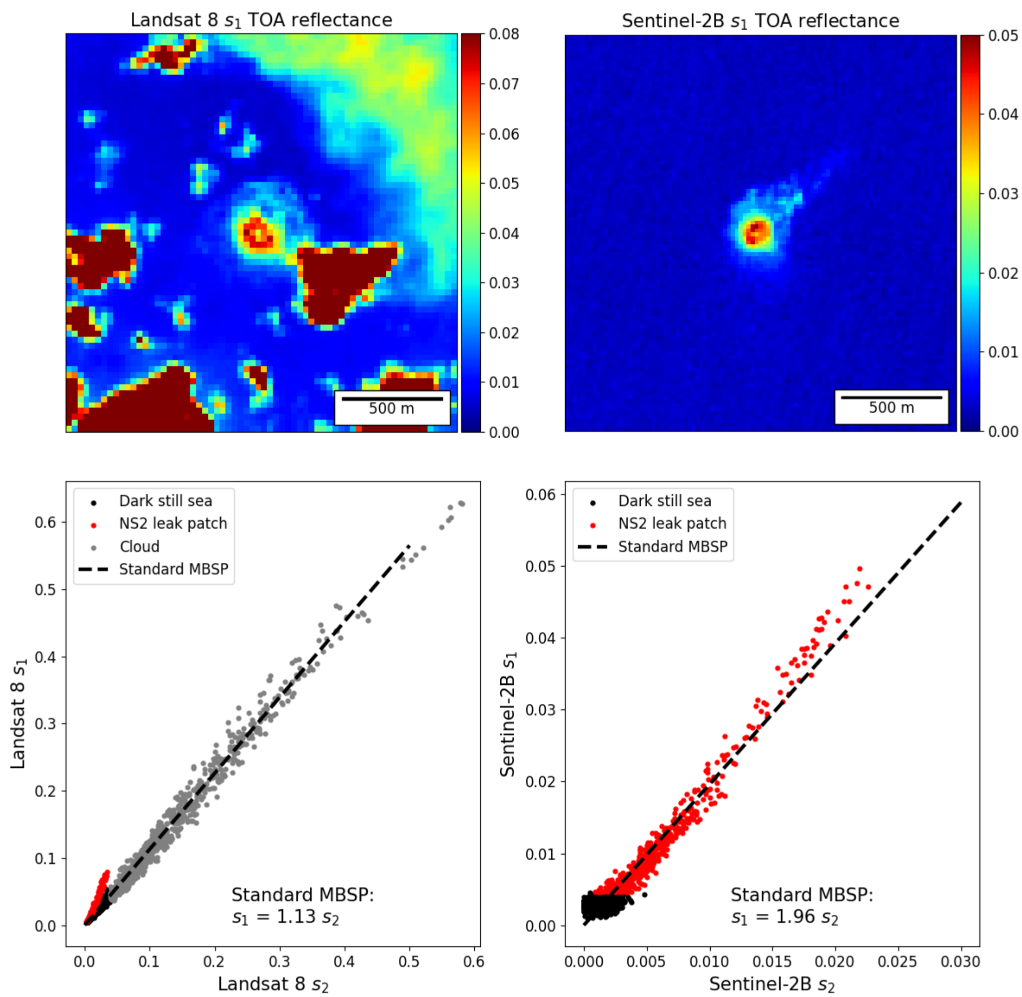

Figure 1: Landsat 8 (left) and Sentinel-2B (right) images of the Nord Stream 2 leak for s_1 (top), and s_1 and s_2 TOA reflectance comparisons depicting different pixel natures and showing the standard MBSP c calibration line (bottom).

s_1 and s_2 is critical to obtain non-biased methane enhancements through MBSP.

Whitlock et al. (1982) and Koepke (1984) show that we expect a TOA reflectance ratio s_1/s_2 over sea foam of about 2 or slightly lower (graphical reading). However, the only pixels representative of sea foam that can be observed in L8 and S-2B images of the NS2 leak are the ones caused by the leak itself, above which we also expect a possible methane enhancement signal. Unlike a land image, it is thus not possible to assess whether the standard MBSP calibration can separate the spectral impact of methane from the spectral dependence of the albedo for this specific NS2 case. This is particularly noticeable in Fig. 1 for the S-2B image, where the standard MBSP calibration is driven by the NS2 sea foam patch ($c = 1.96$). This issue similarly applies to the L8 NS2 observation, that also features an additional complication: very bright clouds are present in the image, which in this case drive the standard MBSP calibration ($c = 1.13$). The NS2 observation case that relies on a small sea foam patch thus calls for an external calibration of the spectral dependence of sea foam albedo.

We therefore empirically constrain the spectral dependence of sea foam albedo by using sea foam observations in ship trails unaffected by methane plumes. We treat each satellite separately in order to account for their different instrumental characteristics. By visual inspection of RGB Sentinel-2 and Landsat data on the EO Browser of Sentinel-Hub (2023), we gather 27 and 38 images of ship trails for L8 and S-2B, respectively, located in the North and Baltic Seas from September and October 2022. For each of these images, we separate ship and sea foam pixels from the dark still sea pixels by using an empirically determined threshold τ_1, such that $s_1 > \tau_1$; and then separate sea foam from ship pixels by applying a second empirically deter-

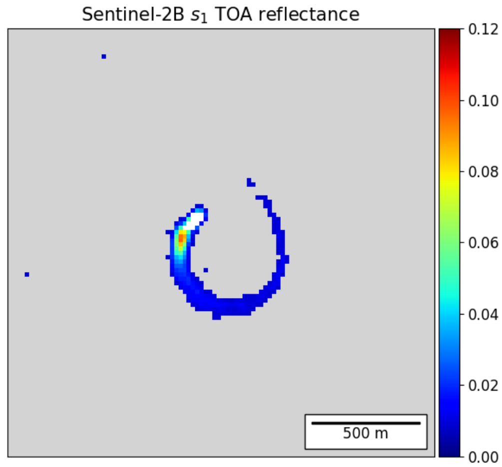

Figure 2: Example of sea foam observation in the Sentinel-2B image of a ship trail. Dark still sea and ship pixels have been removed and are shown in grey and white, respectively.

mined threshold τ_2, such that $s_2 < \tau_2$ (Supplement Tables 2 and 3). Figure 2 shows an example of sea foam pixels extracted from an S-2B ship trail image. For each image, using sea foam pixels only, we perform a least-squares linear fit (with an intercept set to zero) of s_1 as a function of s_2 to determine c_i, the coefficient describing the spectral dependence of sea foam albedo for the i-th image (see individual fits in the Supplements). For L8 and S-2B separately, we then compute $\bar{c}$ as the mean of the individual calibrations. Figure 3 presents the results of this satellite-specific empirical calibration of the spectral dependence of sea foam albedo. We obtain $\bar{c} = 1.96 \pm 0.23$ and $\bar{c} = 1.91 \pm 0.22$ for L8 and S-2B, respectively. These are consistent with results presented by Whitlock et al. (1982) and Koepke (1984). Comparing the S-2B result to the slightly higher standard MBSP calibration ($c = 1.96$) also confirms the above mentioned hypothesis that the standard calibration may have captured some methane signal. Indeed, for given fixed $\{s_1, s_2\}$ values, a decrease in the spectral dependence calibration coefficient c (compared to the standard calibration) reduces $\Delta R = (cs_2 - s_1)/s_1$, which translates to an increase of methane enhancement through MBSP.

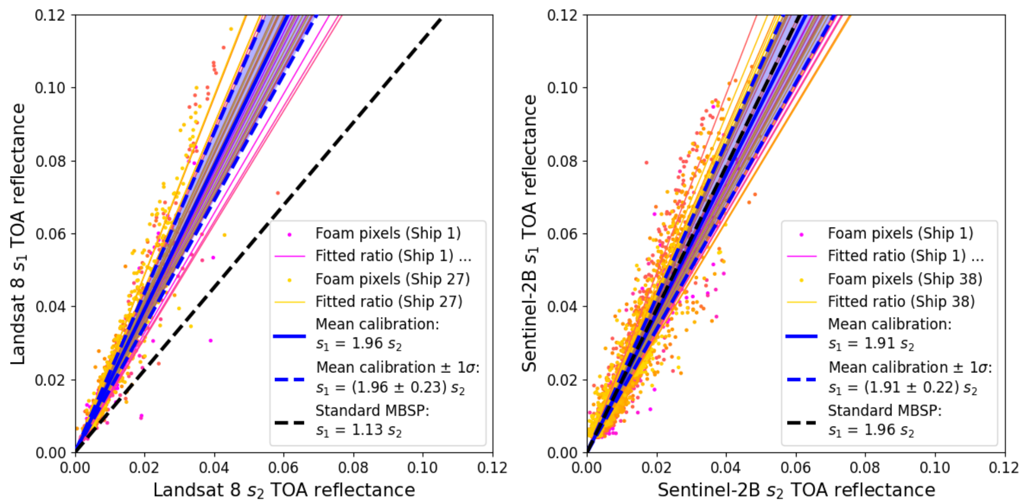

Figure 3: Empirically determined sea foam albedo spectral dependence between s_1 and s_2 for Landsat 8 (left) and Sentinel-2B (right). Sea foam pixels for all ship images are depicted (dots with different colors indicating different ships), along with their respective calibration slopes (thin lines). The mean and 1-σ standard deviation of the empirically determined sea foam albedo spectral dependence are shown (thick full and dashed blue lines), along with the standard MBSP calibration (thick dashed black line).

MBSP can then be applied using these newly determined empirical calibrations (computing ΔR using $\bar{c}$). Figure 4 shows the methane enhancements obtained with the satellite-specific $\bar{c}$ calibration values, and how s_1 and s_2 TOA reflectance values compare to them. For the L8 observation of the NS2 leak, the sea foam patch pixels show an s_1/s_2 ratio of 2.09 (red line), which is slightly higher than the average empirical calibration of the L8 sea foam

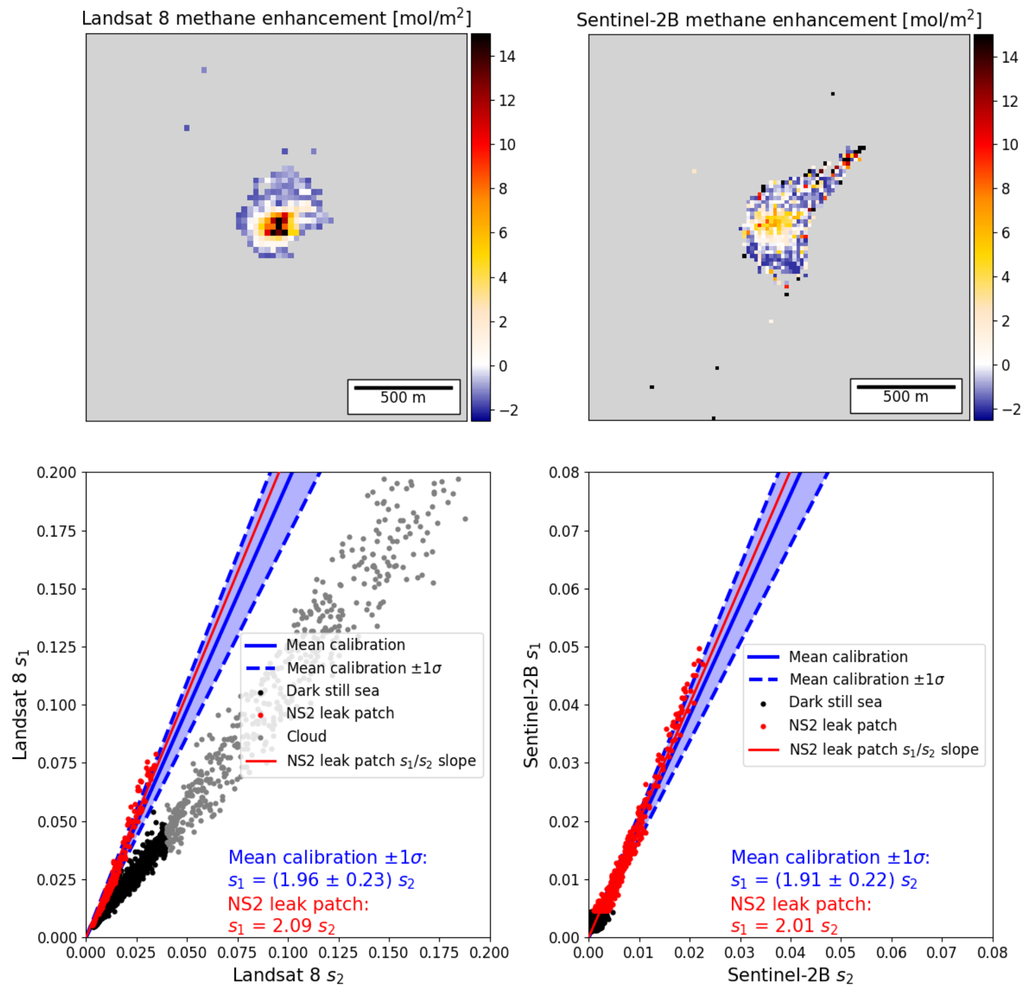

Figure 4: Methane enhancement results obtained through MBSP for Landsat 8 (top left) and Sentinel-2B (top right), pixels not belonging to the foam patch have been filtered out and shown in grey. Comparisons of s_1 and s_2 TOA reflectance (bottom) depicting different pixel types and showing the empirically determined spectral dependence of sea foam albedo (thick blue line), and the s_1/s_2 ratio observed over the NS2 sea foam patch (red line).

albedo spectral dependence ($\bar{c} = 1.96 \pm 0.23$), but comprised within its $\pm 1\sigma$ uncertainty interval. This negative difference overall translates to positive methane enhancement through MBSP. On average, we obtain L8 methane enhancement values ranging from -2.5 to 15 mol/m^2. Negative enhancements are associated with pixels falling right of the s_1/s_2 empirical calibration line (low TOA reflectance values, at the sea foam patch edges), and positive enhancements are associated with pixels falling left of the empirical calibration line (high TOA reflectance values, at the sea foam patch center). The S-2B observation is similar but exhibits more noise, overall showing enhancements from -2.5 mol/m^2 on the sea foam patch edges to about 8 mol/m^2 at its brighter center.

3.3. Effective wind calibration of partial plume observation in IME

The IME method is critically sensitive to the plume mask extent. For a homogeneous plume of N pixels, the source rate Q increases linearly with $\sqrt{N}$. In practice, the plume is not homogeneous and the number of pixels above the instrument detection threshold relates to the emission rate, and truncating the plume mask because of external factors (low albedo, clouds, etc.) biases Q. This IME sensitivity stems from the effective wind speed calibration that relies on an LES sampling of whole plume per the given instrument characteristics. Any systematic plume mask truncation therefore needs to be calibrated for. For the NS2 observation, only the small sea foam patch provides a high enough signal that could allow observation of part of the methane plume, above its source. This specific case therefore requires a custom effective wind calibration.

We consequently re-purpose an ensemble of LES simulations computed for a 275×275 m^2 source area (grossly the NS2 foam patch size) by Maasakkers et al. (2022), scale them to emission rates ranging from 100 to 1000 t/hr, resample them according to L8/S-2B instrumental characteristics and perform an effective wind speed calibration that only includes the pixels located above the source area in the plume mask. We obtain the following NS2-custom effective wind speed calibration with an outlier-resilient Huber regression: $U_{\text{eff}} = 1.88 \times U_{10\text{m}} + 0.52$. This 1.88 calibration factor, close to 2, is consistent with expectations from mass balance of a uniformly ventilated area source as shown by Buchwitz et al. (2017), and is significantly different from the slope value given in Sect. 2.3, applicable for ideal conditions over land.

4. Methane emission rates from Nord Stream 2 leak as seen by Landsat 8 and Sentinel-2B

We use an ensemble approach to calculate the average methane leak rate from NS2, as seen by L8 and S-2B, using MBSP and IME with our custom calibrations.

4.1. Ensemble approach

To estimate uncertainty, we perturb six different parameters that impact MBSP and/or IME results to generate an ensemble of leak rate quantifications:

(1) In MBSP, we perturb the empirical calibration of the spectral dependence of sea foam albedo determined in Sect. 3.2 by $\pm 1\sigma$ in 0.1σ steps.

(2) To capture the uncertainty in the background, we estimate a non-enhanced methane background over the NS2 sea foam patch. It is computed by applying MBSP using a calibration coefficient exactly equal to the fitted

s_1/s_2 ratio obtained from the NS2 sea foam pixels, thus fully compensating for possible methane enhancements. We then compute the standard deviation $\sigma_{X_{CH_4}}$ of this background signal, and use it to shift the MBSP enhancement results by $\pm 1\sigma_{X_{CH_4}}$ in $0.1\sigma_{X_{CH_4}}$ steps.

(3) We perturb the plume mask extent by varying the minimum s_1 TOA reflectance value for a pixel to be included in the plume mask. These minimum s_1 TOA reflectance thresholds cover $[0, 0.07]$ for L8 and $[0, 0.045]$ for S-2B, with 0.005 steps for both satellites. We use different maximum thresholds for each satellite because the maximum TOA reflectance observed by L8 in the NS2 patch is higher than for S-2B (see Fig. 1).

(4) We include four different 10-m wind speeds. Three come from meteorological re-analysis products: the European Centre for Medium-Range Weather Forecasts (ECMWF) ERA5 (Hersbach et al., 2020), the Global Forcasting System (GFS) from NOAA National Centers for Environmental Prediction (NCEP, 2000) and the Goddard Earth Observing System-Forward Processing (GESO-FP, Molod et al., 2012). Furthermore, we include the insitu wind speed measured at Bornholm airport, which is located about 50 km away from the NS2 leak (IEM, 2023). For September 29$^{\text{th}}$, we obtain wind speeds of 4.1, 6.6, 4.8 and 3.6 m/s from ERA5, GFS, GEOS-FP and airport measurements, respectively; and for September 30$^{\text{th}}$, we obtain wind speeds of 5.0, 6.3, 6.3 and 5.7 m/s, respectively.

(5) We perturb wind speed values by ±50%, with 10% steps.

(6) We perturb effective wind speed calibration coefficients by ±5%, with 1% steps.

Overall, we get 3,201,660 and 2,134,440 ensemble members for L8 and

S-2B, respectively, and report their standard deviations as uncertainty.

4.2. Results and discussion

Figure 5 shows the distribution of leak rate values within the ensembles for L8 and S-2B. We obtain ensemble-averaged methane leak rates of 433 ± 459 t/hr and 398 ± 449 t/hr for L8 and S-2B, respectively. These $\pm 1\sigma$ uncertainty intervals are mainly driven by the perturbation of the empirical calibration of sea foam albedo spectral dependence (color scale in Fig. 5), and by the shift in the methane background. Leak rates get lower and eventually negative with increasing empirical sea foam albedo spectral dependence calibration values.

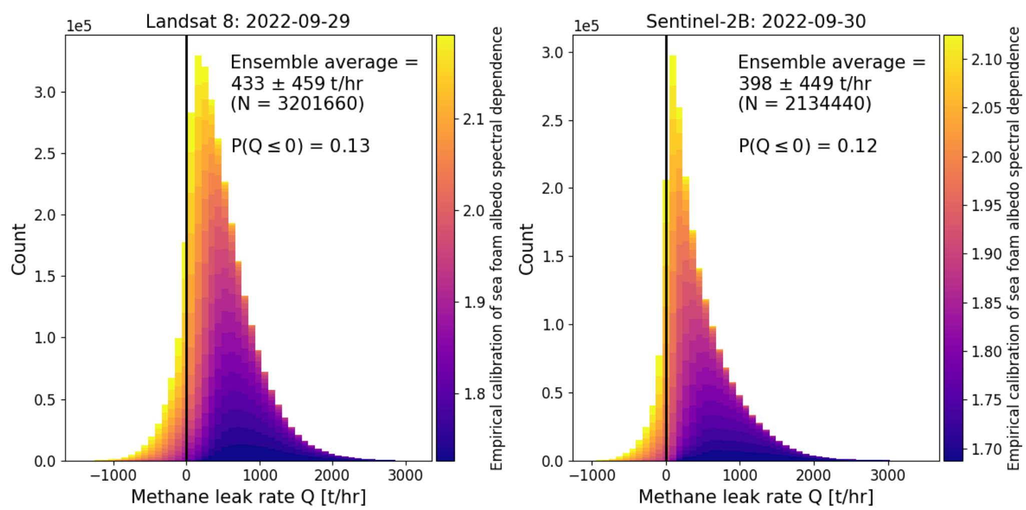

Figure 5: Distributions of methane emission rate values for the Landsat 8 (left) and Sentinel-2B (right) ensembles. Ensemble means and standard deviations are shown inset, along with the fraction of null or negative emission rates. The color scale shows the contributions of different sea foam albedo spectral dependence calibration values to the overall distribution of leak rates within the ensemble.

The individual L8 and S-2B ensemble distributions have $\pm 1\sigma$ uncertainty intervals that include zero emissions, and show $P(Q \leq 0) = 0.13$ and $P(Q \leq 0) = 0.12$, respectively. Consequently, considering these null-hypothesis probabilities higher than 10%, no firm conclusion can be drawn regarding separate L8 and S-2B detections of the NS2 methane leak.

Because this NS2 observation case is singular and recent, very few results to compare to have been published. GHGSat reports leak rates of 79 t/hr and 29 t/hr for their NS2 glint observations made on Sept 30$^{\text{th}}$ (GHGSat, 2022). Jia et al. (2022) report no result for L8, and a methane leak rate of 72 ± 38 t/hr for S-2B, while also acknowledging significant uncertainties in their methodology regarding the spectral reflectance of bubbles and the partial imaging of the methane plume. The work performed here precisely describes the origin of the challenges posed by these specific NS2 observations, and addresses them through custom calibrations. All previously reported NS2 methane leak rates for September 30$^{\text{th}}$ are comprised within our large zero-including uncertainty range obtained for S-2B on that day.

If we opportunistically assume that the L8 and S-2B leak rate quantifications are independent (different satellites, but an identical method to process observations), we can generate an ensemble representing the averaged combined L8 and S-2B NS2 leak rate. Because distributions in Fig 5 are not Gaussian, we perform 100 random draws of 1M elements from the separate individual L8 and S-2B ensembles, from which we compute 1M element-wise averaged leak rates. On average, we obtain an averaged L8 and S-2B NS2 methane leak rate of 415 ± 321 t/hr, with $P(Q \leq 0) = 0.06$. Thus, under this favorable assumption, considering the null-hypothesis probability lower than

10%, these results give weak confidence that the dual-overpass combination of L8 and S-2B has indeed detected the NS2 methane leak.

5. Conclusions

We have evaluated the possibility of extracting methane emission information from Landsat 8 (L8) and Sentinel-2B (S-2B) observations of the Nord Stream 2 (NS2) pipeline leak.

We have shown how the unusual observations of a sea foam patch surrounded by dark still sea (and clouds for L8) challenge implicit underlying hypotheses in both the Multi-Band Single-Pass (MBSP) and Integrated Mass Enhancement (IME) methods. For MBSP, we showed an external empirical calibration of the sea foam albedo spectral dependence is needed, and provided one by using sea foam observations in ship trails. For IME, we showed that emission rate quantifications are critically sensitive to plume mask truncation, and we provided an effective wind speed calibration customized to the NS2 leak, that is only observed over a small sea foam patch.

Using these two-fold customized calibrations for MBSP and IME in an ensemble approach, we have assessed that no firm conclusion can be made about individual L8 and S-2B detection of the NS2 methane leak. If we opportunistically assume that they are independent, we obtain an averaged dual-overpass (L8 and S-2B combined) NS2 methane leak rate of 415 ± 321 t/hr, with only a small null-hypothesis probability $P\,(Q \leq 0) = 0.06$.

Our work illustrates how implicit method hypotheses need to be considered and compensated for in unusual observation cases such as this one. Our nuanced results with large uncertainties are not surprising: this exceptional Nord Stream leak event pushed Earth imagers that were not initially designed to observe greenhouse gases - even less over water - to their very limits.

Data availability

Landsat 8 and Sentinel-2B data used in this work are publicly available and were retrieved from the Google Earth Engine as 2 km-side square images of given targets, from collections `LANDSAT/LC08/C02/T1_TOA` and `COPERNICUS/S2_HARMONIZED`, respectively. All images are listed in the Supplements.

Author contributions

MD and JDM conceived the study. MD performed the satellite data analysis and emission rate quantifications, with supervision from JDM and IA. DJV performed the tailored Nord Stream 2 effective wind speed calibration. MD wrote this Short Communication with feedback from all co-authors.

Declaration of competing interest

The authors declare they have no competing interest.

Acknowledgments

This work is in part supported through the ESA funded MethaneCamp project. Copernicus (modified) Sentinel-2 data (2022) have been used. Authors are grateful to Itziar Irakulis-Loitxate and Otto Hasekamp for the helpful discussions and comments while designing this work.

References

Buchwitz, M., Schneising, O., Reuter, M., Heymann, J., Krautwurst, S., Bovensmann, H., Burrows, J.P., Boesch, H., Parker, R.J., Somkuti, P., Detmers, R.G., Hasekamp, O.P., Aben, I., Butz, A., Frankenberg, C., Turner, A.J., 2017. Satellite-derived methane hotspot emission estimates using a fast data-driven method. Atmospheric Chemistry and Physics 17, 5751–5774. URL: https://acp.copernicus.org/articles/17/5751/2017/, doi:10.5194/acp-17-5751-2017.

Drusch, M., Del Bello, U., Carlier, S., Colin, O., Fernandez, V., Gascon, F., Hoersch, B., Isola, C., Laberinti, P., Martimort, P., Meygret, A., Spoto, F., Sy, O., Marchese, F., Bargellini, P., 2012. Sentinel-2: ESA's Optical High-Resolution Mission for GMES Operational Services. Remote Sensing of Environment 120, 25–36. URL: https://www.sciencedirect.com/science/article/pii/S0034425712000636, doi:https://doi.org/10.1016/j.rse.2011.11.026. the Sentinel Missions - New Opportunities for Science.

Frankenberg, C., Thorpe, A.K., Thompson, D.R., Hulley, G., Kort, E.A., Vance, N., Borchardt, J., Krings, T., Gerilowski, K., Sweeney, C., Conley, S., Bue, B.D., Aubrey, A.D., Hook, S., Green, R.O., 2016. Airborne methane remote measurements reveal heavy-tail flux distribution in Four Corners region. Proceedings of the National Academy of Sciences 113, 9734–9739.

URL: https://www.pnas.org/doi/abs/10.1073/pnas.1605617113, doi:10.1073/pnas.1605617113.

GHGSat, 2022. GHGSat measures its largest emission from a single source ever from Nord Stream 2 leak. URL: https://www.ghgsat.com/en/newsroom/ghgsat-nordstream/. accessed: 2023-05-10.

Hersbach, H., Bell, B., Berrisford, P., Hirahara, S., Horányi, A., Muñoz-Sabater, J., Nicolas, J., Peubey, C., Radu, R., Schepers, D., Simmons, A., Soci, C., Abdalla, S., Abellan, X., Balsamo, G., Bechtold, P., Biavati, G., Bidlot, J., Bonavita, M., De Chiara, G., Dahlgren, P., Dee, D., Diamantakis, M., Dragani, R., Flemming, J., Forbes, R., Fuentes, M., Geer, A., Haimberger, L., Healy, S., Hogan, R.J., Hólm, E., Janisková, M., Keeley, S., Laloyaux, P., Lopez, P., Lupu, C., Radnoti, G., de Rosnay, P., Rozum, I., Vamborg, F., Villaume, S., Thépaut, J.N., 2020. The ERA5 global reanalysis. Quarterly Journal of the Royal Meteorological Society 146, 1999–2049. URL: https://rmets.onlinelibrary.wiley.com/doi/abs/10.1002/qj.3803, doi:https://doi.org/10.1002/qj.3803.

IEM, 2023. Asos-awos-metar data download, iowa environmental mesonet (iem). URL: https://mesonet.agron.iastate.edu/ASOS/. accessed: 2023-05-09.

IMEO, 2022. Satellite detects methane plume in Nord Stream leak. URL: https://twitter.com/MethaneData/status/1575610350548164608. accessed: 2023-07-20.

IPCC, 2021. Summary for Policymakers. Cambridge University Press, Cambridge, United Kingdom and New York, NY, USA. pp. 3–32. doi:10.1017/9781009157896.001.

Irakulis-Loitxate, I., Gorroño, J., Zavala-Araiza, D., Guanter, L., 2022a. Satellites Detect a Methane Ultra-emission Event from an Offshore Platform in the Gulf of Mexico. Environmental Science & Technology Letters 9, 520–525. URL: https://doi.org/10.1021/acs.estlett.2c00225, doi:10.1021/acs.estlett.2c00225.

Irakulis-Loitxate, I., Guanter, L., Maasakkers, J.D., Zavala-Araiza, D., Aben, I., 2022b. Satellites Detect Abatable Super-Emissions in One of the World's Largest Methane Hotspot Regions. Environmental Science & Technology 56, 2143–2152. URL: https://doi.org/10.1021/acs.est.1c04873, doi:10.1021/acs.est.1c04873. pMID: 35102741.

Jervis, D., McKeever, J., Durak, B.O.A., Sloan, J.J., Gains, D., Varon, D.J., Ramier, A., Strupler, M., Tarrant, E., 2021. The ghgsat-d imaging spectrometer. Atmospheric Measurement Techniques 14, 2127–2140. URL: https://amt.copernicus.org/articles/14/2127/2021/, doi:10.5194/amt-14-2127-2021.

Jia, M., Li, F., Zhang, Y., Wu, M., Li, Y., Feng, S., Wang, H., Chen, H., Ju, W., Lin, J., Cai, J., Zhang, Y., Jiang, F., 2022. The Nord Stream pipeline gas leaks released approximately 220,000 tonnes of methane into the atmosphere. Environmental Science and Ecotechnology 12, 100210. URL: https://www.sciencedirect.com/science/article/pii/S2666498422000667, doi:https://doi.org/10.1016/j.ese.2022.100210.

Koepke, P., 1984. Effective reflectance of oceanic whitecaps. Appl. Opt. 23, 1816–1824. URL: https://opg.optica.org/ao/abstract.cfm?URI=ao-23-11-1816, doi:10.1364/AO.23.001816.

Lauvaux, T., Giron, C., Mazzolini, M., d'Aspremont, A., Duren, R., Cusworth, D., Shindell, D., Ciais, P., 2022. Global assessment of oil and gas methane ultra-emitters. Science 375, 557–561. URL: https://www.science.org/doi/abs/10.1126/science.abj4351, doi:10.1126/science.abj4351.

Lorente, A., Borsdorff, T., Butz, A., Hasekamp, O., aan de Brugh, J., Schneider, A., Wu, L., Hase, F., Kivi, R., Wunch, D., Pollard, D.F., Shiomi, K., Deutscher, N.M., Velazco, V.A., Roehl, C.M., Wennberg, P.O., Warneke, T., Landgraf, J., 2021. Methane retrieved from TROPOMI: improvement of the data product and validation of the first 2 years of measurements. Atmospheric Measurement Techniques 14, 665–684. URL: https://amt.copernicus.org/articles/14/665/2021/, doi:10.5194/amt-14-665-2021.

Maasakkers, J.D., Varon, D.J., Elfarsdóttir, A., McKeever, J., Jervis, D., Mahapatra, G., Pandey, S., Lorente, A., Borsdorff, T., Foorthuis, L.R., Schuit, B.J., Tol, P., van Kempen, T.A., van Hees, R., Aben, I., 2022. Using satellites to uncover large methane emissions from landfills. Science Advances 8, eabn9683. URL: https://www.science.org/doi/abs/10.1126/sciadv.abn9683, doi:10.1126/sciadv.abn9683.

Molod, A., Takacs, L., Suarez, M., Bacmeister, J., Song, I.S., Eichmann, A., 2012. The GEOS-5 Atmospheric General Circulation Model: Mean Climate and Development from MERRA to Fortuna. Technical Report. NASA. URL: https://ntrs.nasa.gov/citations/20120011790.

NCEP, 2000. NCEP FNL Operational Model Global Tropospheric Analyses. Technical Report. doi:https://doi.org/10.5065/D6M043C6.

Nisbet, E.G., Fisher, R.E., Lowry, D., France, J.L., Allen, G., Bakkaloglu, S., Broderick, T.J., Cain, M., Coleman, M., Fernandez, J., Forster, G., Griffiths, P.T., Iverach, C.P., Kelly, B.F.J., Manning, M.R., Nisbet-Jones, P.B.R., Pyle, J.A., Townsend-Small, A., al Shalaan, A., Warwick, N., Zazzeri, G., 2020. Methane mitigation: Methods to reduce emissions, on the path to the paris agreement. Reviews of Geophysics 58, e2019RG000675. URL: https://agupubs.onlinelibrary.wiley.com/doi/abs/10.1029/2019RG000675, doi:https://doi.org/10.1029/2019RG000675. e2019RG000675 2019RG000675.

Pandey, S., Gautam, R., Houweling, S., van der Gon, H.D., Sadavarte, P., Borsdorff, T., Hasekamp, O., Landgraf, J., Tol, P., van Kempen, T., Hoogeveen, R., van Hees, R., Hamburg, S.P., Maasakkers, J.D., Aben, I., 2019. Satellite observations reveal extreme methane leakage from a natural gas well blowout. Proceedings of the National Academy of Sciences 116, 26376–26381. URL: https://www.pnas.org/doi/abs/10.1073/pnas.1908712116, doi:10.1073/pnas.1908712116.

Roy, D., Wulder, M., Loveland, T., C.E., W., Allen, R., Anderson, M., Helder, D., Irons, J., Johnson, D., Kennedy, R., Scambos, T., Schaaf, C., Schott, J., Sheng, Y., Vermote, E., Belward, A., Bindschadler, R., Cohen, W., Gao, F., Hipple, J., Hostert, P., Huntington, J., Justice, C., Kilic, A., Kovalskyy, V., Lee, Z., Lymburner, L., Masek, J., McCorkel, J., Shuai, Y., Trezza, R., Vogelmann, J., Wynne, R., Zhu, Z., 2014. Landsat-8: Science and product vision for terrestrial global change research. Remote Sensing of Environment 145, 154–172. URL: https://www.sciencedirect.com/science/article/pii/S003442571400042X, doi:https://doi.org/10.1016/j.rse.2014.02.001.

Sanderson, K., 2022. What do Nord Stream methane leaks mean for climate change? URL: https://www.nature.com/articles/d41586-022-03111-x, doi:https://doi.org/10.1038/d41586-022-03111-x. accessed: 2023-05-10.

Schuit, B.J., Maasakkers, J.D., Bijl, P., Mahapatra, G., Van den Berg, A.W., Pandey, S., Lorente, A., Borsdorff, T., Houweling, S., Varon, D.J., McKeever, J., Jervis, D., Girard, M., Irakulis-Loitxate, I., Gorroño, J., Guanter, L., Cusworth, D.H., Aben, I., 2023. Automated detection and monitoring of methane super-emitters using satellite data. Atmospheric Chemistry and Physics Discussions 2023, 1–47. URL: https://acp.copernicus.org/preprints/acp-2022-862/, doi:10.5194/acp-2022-862.

Sentinel-Hub, 2023. EO Browser. URL: https://apps.sentinel-hub.com/eo-browser. accessed: 2023-07-21.

Varon, D.J., Jacob, D.J., McKeever, J., Jervis, D., Durak, B.O.A., Xia, Y., Huang, Y., 2018. Quantifying methane point sources from fine-scale satellite observations of atmospheric methane plumes. Atmospheric Measurement Techniques 11, 5673–5686. URL: https://amt.copernicus.org/articles/11/5673/2018/, doi:10.5194/amt-11-5673-2018.

Varon, D.J., Jervis, D., McKeever, J., Spence, I., Gains, D., Jacob, D.J., 2021. High-frequency monitoring of anomalous methane point sources with multispectral Sentinel-2 satellite observations. Atmospheric Measurement Techniques 14, 2771–2785. URL: https://amt.copernicus.org/articles/14/2771/2021/, doi:10.5194/amt-14-2771-2021.

Veefkind, J., Aben, I., McMullan, K., Förster, H., de Vries, J., Otter, G., Claas, J., Eskes, H., de Haan, J., Kleipool, Q., van Weele, M., Hasekamp, O., Hoogeveen, R., Landgraf, J., Snel, R., Tol, P., Ingmann, P., Voors, R., Kruizinga, B., Vink, R., Visser, H., Levelt, P., 2012. TROPOMI on the ESA Sentinel-5 Precursor: A GMES mission for global observations of the atmospheric composition for climate, air quality and ozone layer applications. Remote Sensing of Environment 120, 70–83. URL: https://www.sciencedirect.com/science/article/pii/S0034425712000661, doi:https://doi.org/10.1016/j.rse.2011.09.027. the Sentinel Missions - New Opportunities for Science.

Whitlock, C.H., Bartlett, D.S., Gurganus, E.A., 1982. Sea foam reflectance and influence on optimum wavelength for remote sensing of ocean aerosols. Geophysical Research Letters 9, 719–722. URL: https://agupubs.onlinelibrary.wiley.com/doi/abs/10.1029/GL009i006p00719, doi:https://doi.org/10.1029/GL009i006p00719.

Supplementary Materials

Table 1: Nord Stream 2 (NS2) leak satellite images used in this work

Satellite	date	Latitude	Longitude	Filters
Landsat 8	2022-09-29	54.877	15.409	Still sea:
				$s_2 < 0.04$ and $s_1 \leq 1.65\ s_2$
				Clouds: $s_2 \geq 0.04$
				NS2 sea foam:
				$s_2 < 0.04$ and $s_1 > 1.65\ s_2$
Sentinel-2B	2022-09-30	54.877	15.409	Still sea: $s_1 \leq 0.0045$
				NS2 sea foam: $s_1 > 0.0045$

Table 2: Landsat 8 ship trail images used in this work

#	Satellite	date	Latitude	Longitude	τ_1	τ_2
1	Landsat 8	2022-09-02	55.972	11.196	0.0075	0.0400
2	Landsat 8	2022-09-02	54.598	11.305	0.0050	0.0300
3	Landsat 8	2022-09-02	54.268	11.699	0.0050	0.0250
4	Landsat 8	2022-09-06	58.814	18.071	0.0050	0.0300
5	Landsat 8	2022-09-10	59.847	25.522	0.0035	0.0250
6	Landsat 8	2022-09-11	54.527	12.245	0.0040	0.0400
7	Landsat 8	2022-09-11	54.537	12.220	0.0035	0.0200
8	Landsat 8	2022-09-16	57.619	9.834	0.0080	0.0600
9	Landsat 8	2022-09-16	57.627	9.851	0.0070	0.0250
10	Landsat 8	2022-09-16	57.634	9.897	0.0080	0.0300
11	Landsat 8	2022-09-16	57.682	9.814	0.0085	0.0300
12	Landsat 8	2022-09-16	56.734	7.976	0.0080	0.0300
13	Landsat 8	2022-09-25	57.122	10.760	0.0055	0.0300
14	Landsat 8	2022-09-25	54.131	8.013	0.0065	0.0150
15	Landsat 8	2022-10-02	57.574	8.855	0.0075	0.0200
16	Landsat 8	2022-10-02	57.721	8.481	0.0055	0.0200
17	Landsat 8	2022-10-02	57.611	9.921	0.0080	0.0250
18	Landsat 8	2022-10-02	57.563	8.884	0.0065	0.0300

Continued on next page

Table 2: Landsat 8 ship trail images used in this work (Continued)

#	**Satellite**	**date**	**Latitude**	**Longitude**	τ_1	τ_2
19	Landsat 8	2022-10-04	54.461	10.261	0.0080	0.0150
20	Landsat 8	2022-10-06	63.508	20.536	0.0065	0.0300
21	Landsat 8	2022-10-06	54.878	13.070	0.0100	0.0300
22	Landsat 8	2022-10-10	58.846	21.509	0.0070	0.0300
23	Landsat 8	2022-10-15	56.613	17.809	0.0115	0.0300
24	Landsat 8	2022-10-18	57.614	9.918	0.0105	0.0300
25	Landsat 8	2022-10-18	57.674	9.774	0.0100	0.0500
26	Landsat 8	2022-10-20	55.957	11.260	0.0250	0.0350
27	Landsat 8	2022-10-20	55.169	12.888	0.0070	0.0200

Table 3: Sentinel-2B ship trail images used in this work

#	**Satellite**	**date**	**Latitude**	**Longitude**	τ_1	τ_2
1	Sentinel-2B	2022-09-02	56.700	7.823	0.0040	0.0400
2	Sentinel-2B	2022-09-02	56.748	7.958	0.0040	0.0400
3	Sentinel-2B	2022-09-03	54.369	11.981	0.0050	0.0400
4	Sentinel-2B	2022-09-03	54.390	11.992	0.0050	0.0400
5	Sentinel-2B	2022-09-06	56.851	11.812	0.0080	0.0600
6	Sentinel-2B	2022-09-06	56.856	11.840	0.0090	0.0300

Continued on next page

Table 3: Sentinel-2B ship trail images used in this work (Continued)

#	**Satellite**	**date**	**Latitude**	**Longitude**	τ_1	τ_2
7	Sentinel-2B	2022-09-06	57.456	11.453	0.0070	0.0300
8	Sentinel-2B	2022-09-07	54.574	18.878	0.0045	0.0400
9	Sentinel-2B	2022-09-09	55.789	10.741	0.0115	0.0350
10	Sentinel-2B	2022-09-13	54.315	11.833	0.0070	0.0400
11	Sentinel-2B	2022-09-13	54.541	11.410	0.0080	0.0150
12	Sentinel-2B	2022-09-13	54.530	11.427	0.0090	0.0200
13	Sentinel-2B	2022-09-16	56.032	10.737	0.0200	0.0375
14	Sentinel-2B	2022-09-19	57.676	9.673	0.0070	0.0400
15	Sentinel-2B	2022-09-19	57.464	10.935	0.0120	0.0300
16	Sentinel-2B	2022-09-19	57.472	8.615	0.0045	0.0500
17	Sentinel-2B	2022-09-30	54.982	18.303	0.0050	0.0500
18	Sentinel-2B	2022-09-30	54.876	17.373	0.0040	0.0350
19	Sentinel-2B	2022-09-30	54.830	13.773	0.0070	0.0300
20	Sentinel-2B	2022-09-30	54.304	13.980	0.0060	0.0400
21	Sentinel-2B	2022-10-02	57.681	9.873	0.0160	0.0350
22	Sentinel-2B	2022-10-02	57.794	9.230	0.0070	0.0410
23	Sentinel-2B	2022-10-03	54.613	11.309	0.0115	0.0400
24	Sentinel-2B	2022-10-03	54.629	11.311	0.0100	0.0500

Continued on next page

Table 3: Sentinel-2B ship trail images used in this work (Continued)

#	**Satellite**	**date**	**Latitude**	**Longitude**	τ_1	τ_2
25	Sentinel-2B	2022-10-06	54.448	12.055	0.0110	0.0400
26	Sentinel-2B	2022-10-06	54.442	12.008	0.0110	0.0400
27	Sentinel-2B	2022-10-07	54.880	19.232	0.0110	0.0200
28	Sentinel-2B	2022-10-10	55.528	15.159	0.0110	0.0300
29	Sentinel-2B	2022-10-12	57.679	9.650	0.0110	0.0400
30	Sentinel-2B	2022-10-12	57.621	9.932	0.0080	0.0400
31	Sentinel-2B	2022-10-16	54.292	12.024	0.0070	0.0300
32	Sentinel-2B	2022-10-16	54.580	11.277	0.0090	0.0300
33	Sentinel-2B	2022-10-16	54.568	11.278	0.0105	0.0400
34	Sentinel-2B	2022-10-19	57.788	10.140	0.0050	0.0300
35	Sentinel-2B	2022-10-19	57.673	9.715	0.0045	0.0300
36	Sentinel-2B	2022-10-20	54.800	13.774	0.0200	0.0300
37	Sentinel-2B	2022-10-30	56.678	17.251	0.0070	0.0400
38	Sentinel-2B	2022-10-30	55.284	14.162	0.0210	0.0400

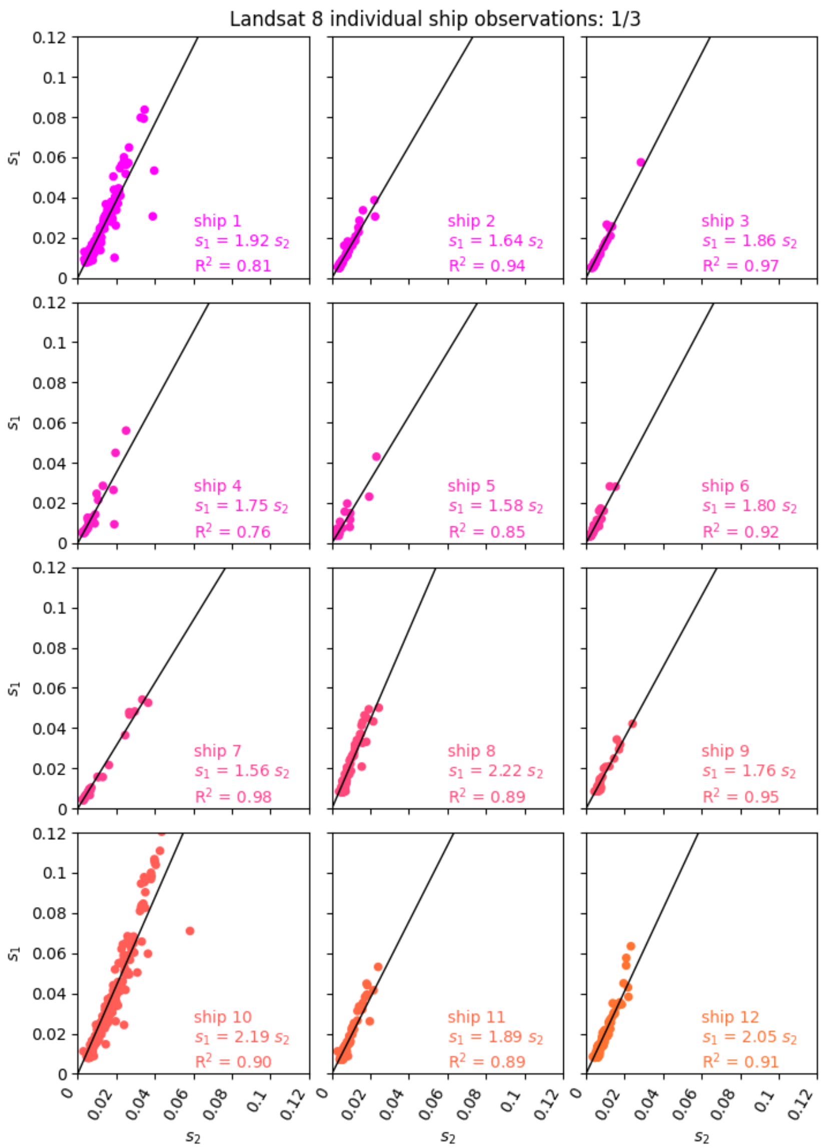

Figure 6: Individual Landsat 8 sea foam observations in ship trails and least-squares linear regression lines with intercepts forced to zero (1/3).

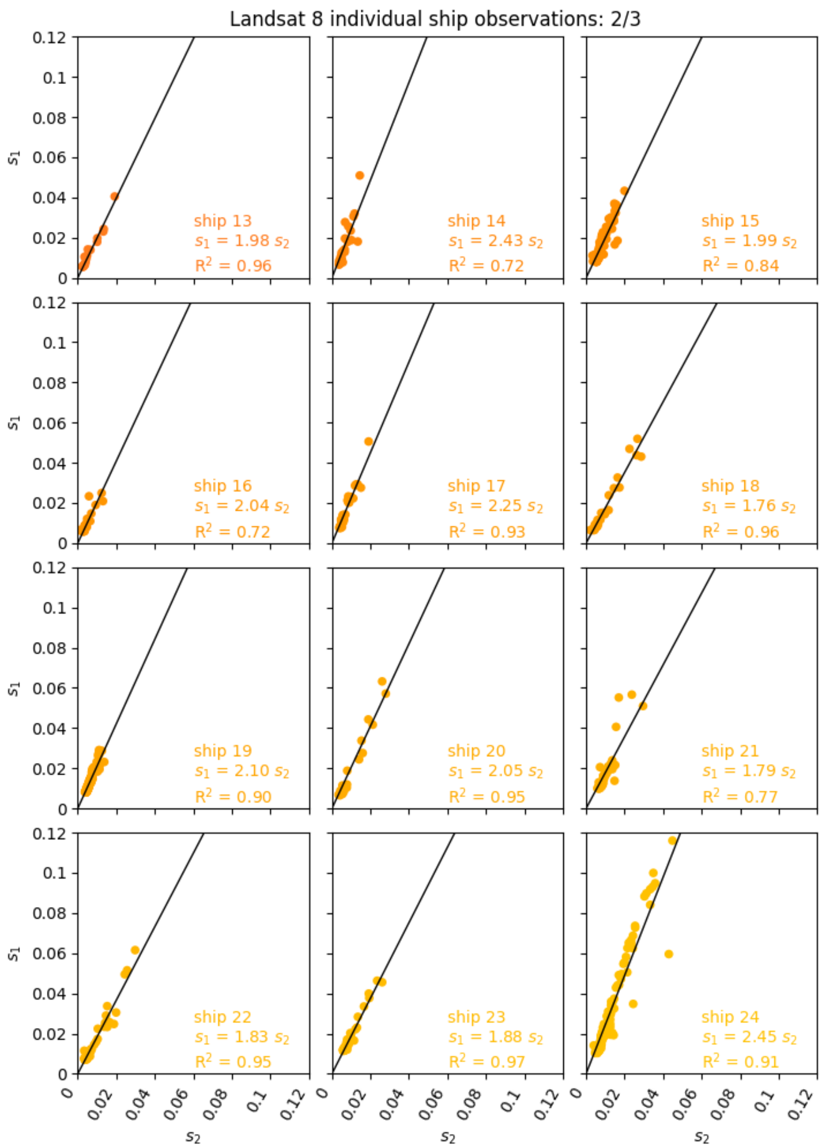

Figure 7: Individual Landsat 8 sea foam observations in ship trails and least-squares linear regression lines with intercepts forced to zero (2/3).

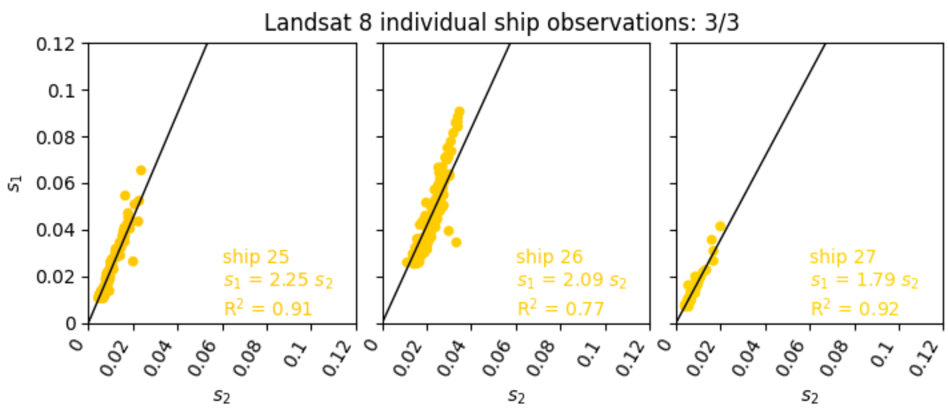

Figure 8: Individual Landsat 8 sea foam observations in ship trails and least-squares linear regression lines with intercepts forced to zero (3/3).

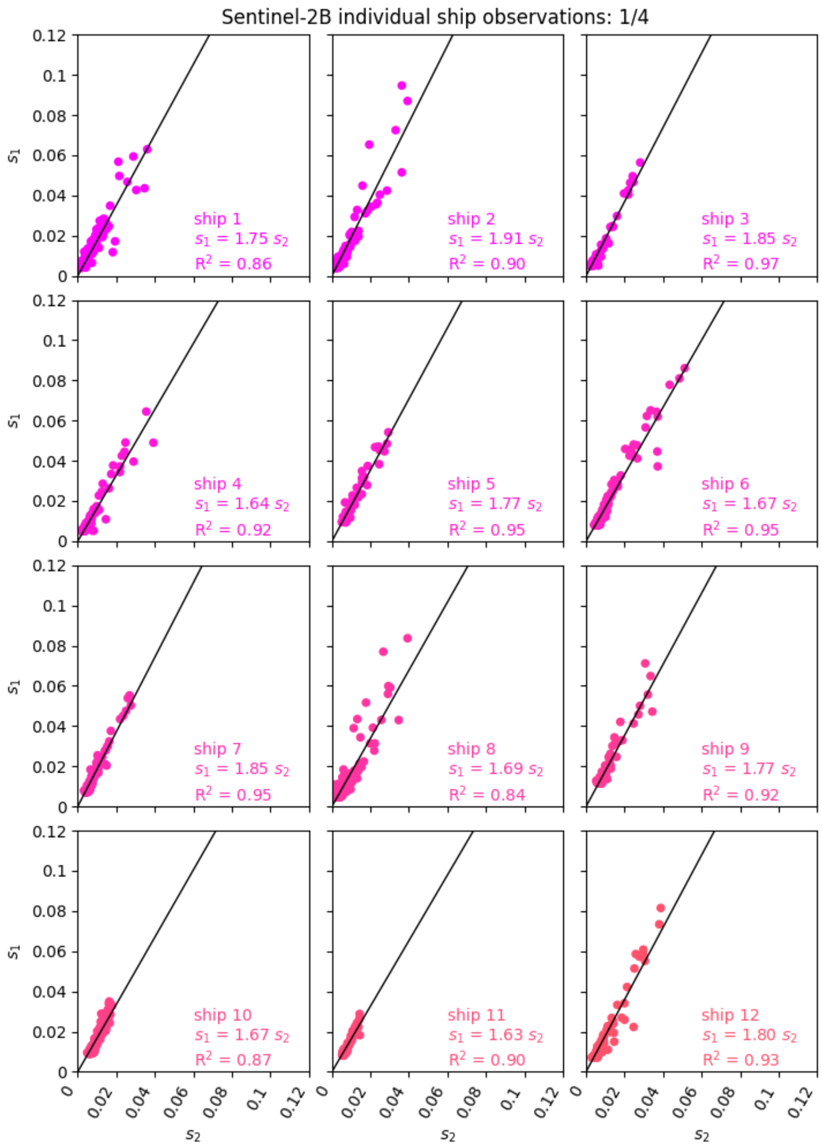

Figure 9: Individual Sentinel-2B sea foam observations in ship trails and least-squares linear regression lines with intercepts forced to zero (1/4).

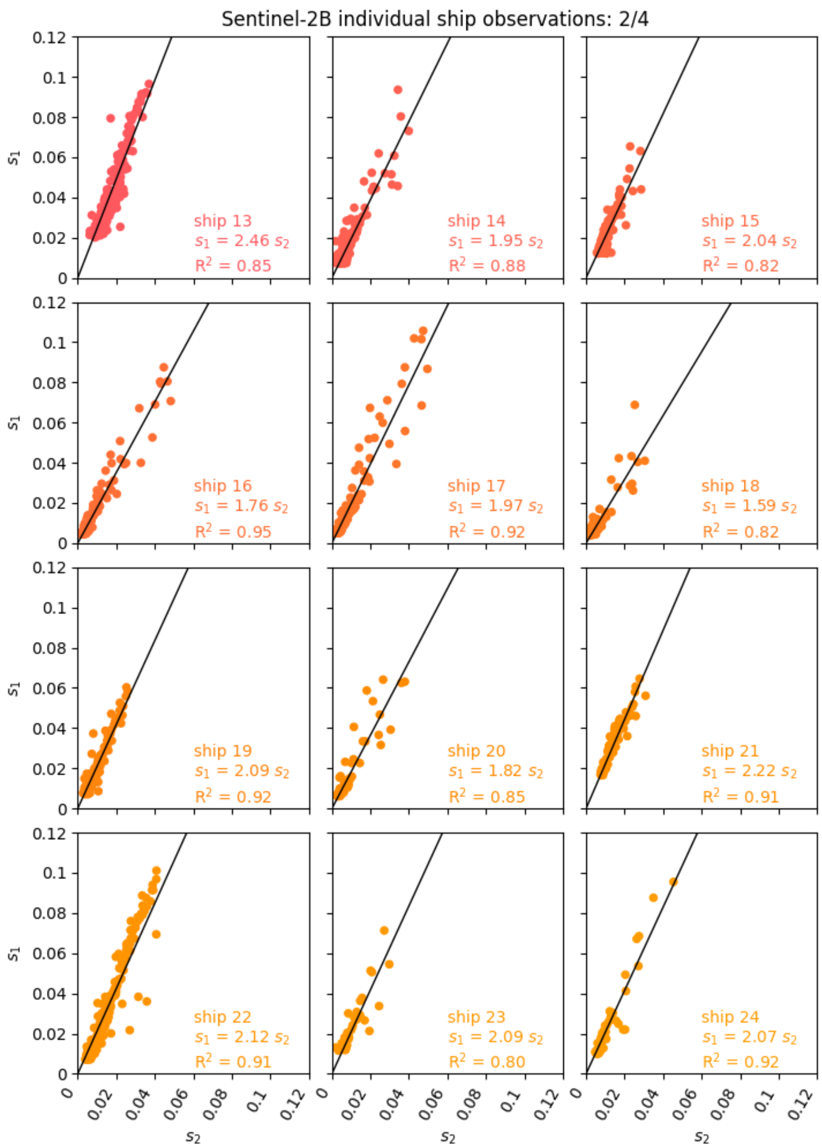

Figure 10: Individual Sentinel-2B sea foam observations in ship trails and least-squares linear regression lines with intercepts forced to zero (2/4).

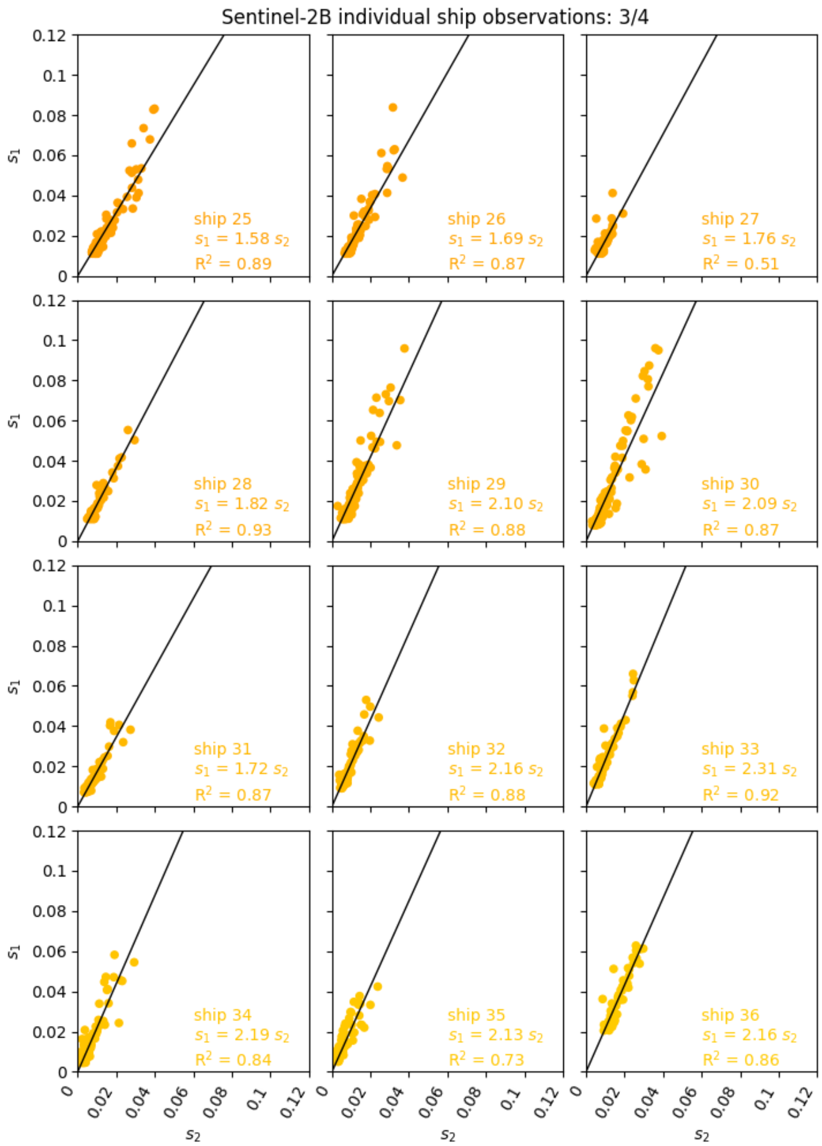

Figure 11: Individual Sentinel-2B sea foam observations in ship trails and least-squares linear regression lines with intercepts forced to zero (3/4).

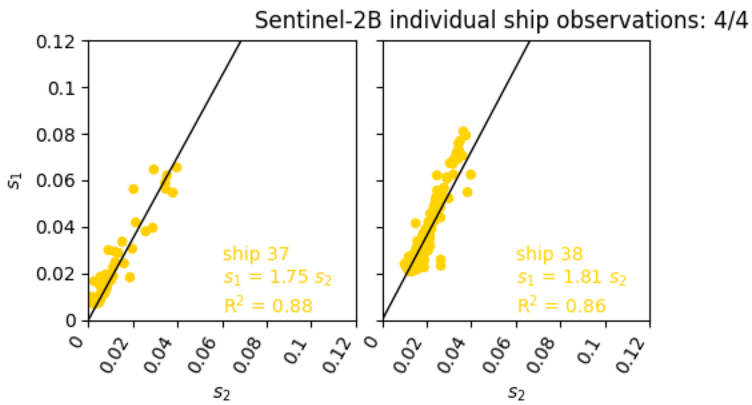

Figure 12: Individual Sentinel-2B sea foam observations in ship trails and least-squares linear regression lines with intercepts forced to zero (4/4).